Ab Initio Molecular Dynamics of Excited-State Intramolecular Proton Transfer around a Three-State Conical Intersection in Malonaldehyde†

Joshua D. Coe and Todd J. Martínez*

Department of Chemistry, Beckman Institute, and Frederick Seitz Materials Research Laboratory, University of Illinois at Urbana-Champaign, 600 South Mathews Avenue, Urbana, Illinois 61801

Received: June 29, 2005; In Final Form: September 28, 2005

Excited-state potential energy surface (PES) characterization is carried out at the CASSCF and MRSDCI levels, followed by ab initio dynamics simulation of excited-state intramolecular proton transfer (ESIPT) on the $S_2(\pi\pi^*)$ state in malonaldehyde. The proton-transfer transition state lies close to an S_2/S_1 conical intersection, leading to substantial coupling of proton transfer with electronic relaxation. Proton exchange proceeds freely on S_2, but its duration is limited by competition with twisting out of the molecular plane. This rotamerization pathway leads to an intersection of the three lowest singlet states, providing the first detailed report of ab initio dynamics around a three-state intersection (3SI). There is a significant energy barrier to ESIPT on S_1, and further pyramidalization of the twisted structure leads to the minimal energy S_1/S_0 intersection and energetic terminal point of excited-state dynamics. Kinetics and additional mechanistic details of these pathways are discussed. Significant depletion of the spectroscopic state and recovery of the ground state is seen within the first 250 fs after photoexcitation.

I. Introduction

Excited-state intramolecular proton transfer (ESIPT)[1,2] is believed to be one of the most rapid events in chemistry ($k_{ESIPT} > 10^{12}$ s^{-1}). Its potential applications range from lasers[3−5] and triplet quenchers[6] to polymer photostabilizers[7−9] and bioluminescence.[10] From an experimental perspective it is uniquely qualified for unambiguous identification—dramatic structural change induces a fluorescence Stokes shift of as much as 6000−12000 cm^{-1} in the product tautomer. In a classic paper published over 50 years ago,[11] Weller attempted to elucidate ESIPT in methyl salicylate (MS) using a zwitterionic mechanism. Although this explanation has since been largely discarded, it established a concrete framework for subsequent inquiry. It is now widely agreed that ESIPT is not well described as *proton* transfer at all, but rather as strongly coupled electron and proton transfer, i.e., hydrogen atom transfer. In keeping with the general consensus regarding malonaldehyde[12] and other ESIPT systems,[1,13] "hydrogen transfer" will be used interchangeably with "proton transfer" in what follows.

There are a wide variety of molecules known to undergo ESIPT, many of which share a 1-hydroxy-2-propenal functional group (the chelate ring conformer of which is commonly referred to as malonaldehyde), as shown in Figure 1. Thus, malonaldehyde (MA) may be viewed as the simplest ESIPT molecule and will be our focus in this paper.

It is clear that there is a barrier to proton transfer on the ground electronic state in MA, and further that there are significant tunneling effects involved in the ground-state reaction. The tunneling splitting has been measured with high accuracy[14,15] and the consensus value is ≈21.6 cm^{-1}. The nature of the reaction coordinate in the excited state has been more controversial. The spectroscopically bright (S_2, $\pi\pi^*$) state lies above a symmetry-forbidden $n\pi^*$ (S_1) state in the Franck−Condon region. Simple chemical intuition might lead one to expect an increased barrier to proton transfer on S_1 because $n\pi^*$ excitation depletes electron density from the carbonyl oxygen, which should serve as proton acceptor. On this basis, Seliskar and Hoffman[16−18] interpreted their linear absorption experiments, which only measure the *difference* in ground and excited-state tunneling splittings, to indicate a decreased tunneling splitting of 7 cm^{-1} for S_1 relative to S_0. As we have already mentioned that ESIPT is not well-described as proton transfer, one might question the chemical intuition that leads to the prediction of an increased barrier. Indeed, subsequent work of Scheiner predicted[19] that the ESIPT reaction would be *barrierless* on both S_1 and S_2. In part due to Scheiner's results, Vaccaro and co-workers[20] interpreted their high-resolution degenerate four-wave mixing experiments to yield an increase in the tunneling splitting of 19 cm^{-1} for S_1 relative to S_0. However, we note that Scheiner used single-reference methods

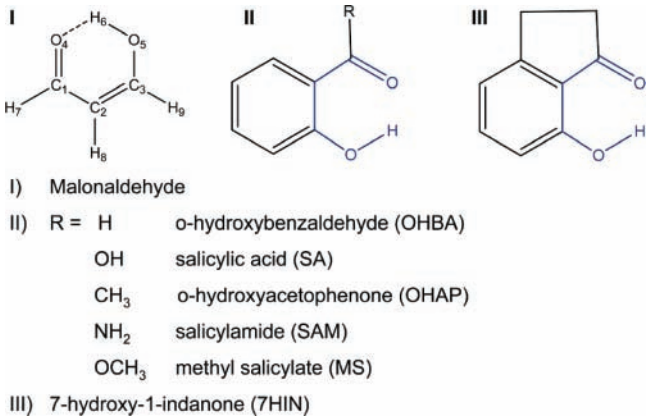

Figure 1. Malonaldehyde and other commonly studied molecules that undergo excited-state intramolecular proton transfer. The recurring malonaldehyde moiety is highlighted in blue. The labeling convention used throughout the text is given in structure **I**.

† Part of the special issue "Donald G. Truhlar Festschrift".

10.1021/jp0535339 CCC: $33.50
Published on Web 11/23/2005

that are not expected to be particularly reliable for describing excited-state potential energy surfaces.[21] More accurate multireference approaches, such as the work of Sobolewski and Domcke[12,22,23] based on complete active space self-consistent field (CASSCF) and CASSCF with perturbation theory corrections for dynamical electron correlation (CASPT2), agree that the reaction is barrierless on S_2 but find a substantial barrier on S_1. In addition, Sobolewski and Domcke speculated as to the existence of an S_2/S_1 conical intersection in close proximity to the hydrogen-transfer transition state. In a recent preliminary communication of the present work, we located not only an S_2/S_1 conical intersection but also a three-state conical intersection where S_0, S_1, and S_2 are simultaneously degenerate.[24]

Although there have been a number of femtosecond time-resolved spectroscopic studies of ESIPT systems such as *o*-hydroxybenzaldehyde (OHBA)[25,26] and methyl salicylate (MS),[27] none have yet been reported for MA. Observed time scales for ESIPT have been reported as 45 (OHBA) and $\leq$60 (MS) fs. It has been suggested[28] that this time scale is dictated by the time required for backbone rearrangement, not the O−H stretch. Both OHBA and MS clearly indicate the opening of radiationless decay channels (to the ground electronic state) at threshold levels of excess vibrational energy. A number of proposals have been offered as to the mechanism[27] underlying this fluorescence quenching, including a possible interaction between the $\pi\pi^*$ state and a higher-lying $\pi\sigma^*$ state.[12] We offer a resolution to this debate on the basis of results detailed below. Attempts to detect fluorescence in MA itself have so far been unsuccessful.[20]

In this paper, we investigate the ultrafast dynamics of ESIPT in MA using first principles dynamics with the ab initio multiple spawning (AIMS) method.[29−31] The electronic structure and quantum wave packet dynamics problems are solved simultaneously. The results of the dynamics are then used to identify important regions of the potential energy surfaces, which are subsequently investigated and verified with more accurate electronic structure methods. Of course, there is no sense in carrying out first principles dynamics if the underlying electronic structure method is inadequate. Hence, we first (section II) provide a survey of important points on the ground- and excited-state potential energy surfaces obtained using time-independent quantum chemistry. Primary emphasis is given to correlating geometric change with the nature of electronic excitation, along with a preliminary dynamical picture based upon energetics of minima, transition states, and surface crossings. Section III begins with a brief overview of our method for studying excited-state dynamics (including nonadiabatic events), to be followed by sampling of the potential energy surface, population flow, kinetics of hydrogen exchange, and dynamics in the presence of a three-state conical intersection. We close with some brief remarks concerning the hydrogen-transfer mechanism and fluorescence quenching in related systems such as OHBA and MS.

II. Electronic Structure

Accurate and efficient ab initio dynamics requires an electronic structure treatment rigorous enough to capture subtleties of the PES (difficult to model with standard force fields) coupled to a dynamical approach avoiding the need for costly integral evaluation. Photo*chemical* processes compound the difficulty in demanding an ansatz whose flexibility is sufficient to accommodate the multiconfigurational character of the electronic wave function at points far from the Franck−Condon region, especially when bond rearrangement occurs.

The most satisfactory balance that we have found so far in meeting the quantum chemical demands is achieved through use of the CASSCF method.[32] Here one sequesters a judiciously chosen set of both occupied and virtual orbitals in which to perform full CI, with the remainder being doubly occupied in all configurations (in the work reported here, all doubly occupied orbitals are optimized unless otherwise noted). The orbitals are optimized to yield the minimum *average* energy of the states under study, eliminating state bias and the corresponding potential for root-flipping.[33,34] In the nomenclature we use in this paper, SA-3-CAS(4/5) denotes full CI in an active space of 4 electrons and 5 orbitals, the orbitals being optimized to minimize the state-averaged energy of the lowest three singlet electronic states.

In addition to an accurate portrayal of the energetics of MA we wish to benchmark energy differences for calibration of active spaces small enough for efficient use in ab initio dynamics. Given the importance of transition-state-like structures to the ESIPT process, along with the expected role of nonadiabatic effects involving S_2 and S_1, our list of target active space desiderata includes the following: (1) accuracy in the Franck−Condon region, taking special note of the S_2/S_1 energy gap, (2) accuracy at the transition state, in particular the magnitude of the S_0 barrier, and (3) relative consistency with benchmark calculations, here represented by large active space CASSCF augmented with multireference single and double excitation configuration interaction (MRSDCI). Although CASSCF primarily addresses static correlation, it introduces dynamic correlation in an erratic and highly unpredictable fashion. Large active spaces tend to bias the covalent states and homogenize bond coordination numbers. This is the expected result of an imbalanced description of near degeneracy effects (static correlation) and dynamic correlation. The target active space is then the one that avoids an unbalanced treatment of static and dynamic correlation, meaning the best CAS space will not necessarily be the most chemically intuitive, and certainly not always the largest possible given current computational limitations.

It should be emphasized from the outset that the correct picture is that which would be obtained using a large active space *and* correlation corrections. Such treatment is not computationally feasible for dynamics simulations but *is* possible at isolated single points. Thus, we have used the energy differences resulting from methods including both large active spaces and dynamic correlation corrections as benchmarks by which to gauge the accuracy of the more approximate levels of theory that are feasible within a dynamics context. This is an internal calibration, with no input from experiment and is therefore quite different from a semiempirical approach. We also ensure consistency between the dynamics results obtained using a lower level of theory and higher levels of theory. There are a number of ways to accomplish this, with the simplest being to trace the potential energy surface using the higher level of theory along the path followed by the dynamics. Comparison of the PES along the dynamics path at the higher level with the same PES along the dynamics path at the lower level of theory provides a difficult consistency test—both PESs should be nearly parallel. When the more accurate PES is in qualitative disagreement with the dynamics results, one needs to begin the calibration process anew, with further data points obtained from the preliminary dynamics. In Figure S1 (Supporting Information), we show such a comparison for a representative trajectory basis function, demonstrating that the SA-3-CAS(4/4) wave

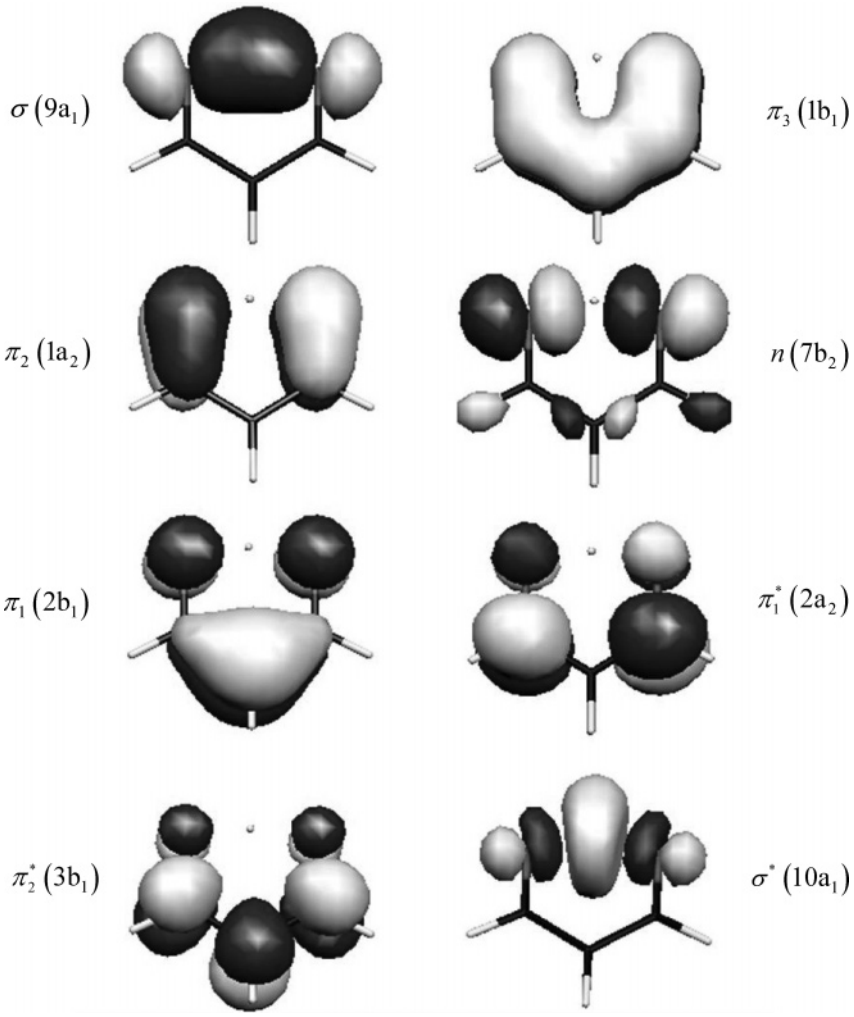

Figure 2. Active space orbitals at the S_0 C_{2v} geometry from CAS(10/8), including the labeling scheme referenced in the text. Symmetry labels are provided in parentheses for ease of comparison with Figure 2 of ref 12. The HOMO and LUMO are π_1 and π_1*, respectively.

function chosen is consistent with the more accurate SA-3-CAS-(4/4)-SDCI wave function.

Figure 2 shows a portion of the orbital set used in our calculations. CAS(4/4) was chosen as a minimal level of treatment for the ground and first two singlet excited states. This active space is composed of the lone pair localized on the O atom participating in the H-bond and three π orbitals concentrated along the backbone (n, π_1, π_1*, and π_2* in Figure 2). CAS(6/6) here includes an additional σ and σ* orbital localized along the O−H−O moiety, the latter deemed by Domcke[12,23] as being essential to a proper description of the ESIPT process. CAS(8/7) is included as an example of an a priori intuitive space in that it includes the entire π manifold (seemingly necessary for a proper description of a coordinated process spanning the whole of the chelate ring), the lone pair orbital, and the σ* orbital. Finally, we have included 10/8 and 14/12 (the "medium" and "extended" spaces of ref 12, respectively) as examples of very large active spaces. The orbitals shown in Figure 2 are generated from CAS(10/8) at the S_0 C_{2v} configuration, i.e., the ground-state proton-transfer barrier.

All calculations were performed using a 6-31G* basis set. Energies at various points were compared to an array of larger sets, including addition of both polarization and diffuse functions. The S_0 minimum geometry was optimized using BLYP, yielding a result very similar to that of MP2.[35] Geometrical parameters for all three of the resulting C_s structures are listed in Table 1, accompanied by the labeling convention shown in

TABLE 1: Comparison of Geometrical Parameters for MP2 and BLYP Optimized S_0 Minima with Those of the Experimentally Determined Structure

parameter	expt	MP2	BLYP
C_1-C_2	1.348	1.364	1.367
C_2-C_3	1.454	1.443	1.440
C_1-O_4	1.320	1.333	1.322
C_3-O_5	1.234	1.250	1.244
O_4-H_6	0.969	1.000	1.004
O_5-H_6	1.708	1.738	1.692
C_1-H_7	1.089	1.088	1.088
C_2-H_8	1.091	1.083	1.083
C_3-H_9	1.094	1.103	1.105
$\angle C_1C_2C_3$	119.4	120.0	119.4
$\angle O_4C_1C_2$	124.5	124.9	124.4
$\angle O_5C_3C_2$	123.0	123.7	123.6
$\angle H_6O_4C_1$	106.3	105.9	105.9
$\angle H_7C_1C_2$	122.3	122.6	122.6
$\angle H_8C_2C_1$	128.1	119.7	120.1
$\angle H_9C_3C_2$	117.6	117.6	117.6

Figure 1. Discounting the $H_8C_2C_1$ angle, which is known to be inaccurately given by the experiment,[14] the theoretical and experimental values are in excellent agreement. An important feature of BLYP optimization is that it correctly reproduces the contraction in H-bond length which is known to be a consequence of dynamic electron correlation.[36] This feature is *not* reflected in ground-state structures optimized using CASSCF, making them undesirable as starting points for dynamics. The Franck−Condon (FC) geometry referenced in the following

TABLE 2: Malonaldeyde Excitation Energies and S_0 Proton-Transfer Barrier Heights (eV)

	$\Delta E_{S_1/S_0}$	$\Delta E_{S_2/S_0}$	$\Delta E_{S_2/S_1}$	S_0 barrier
expt	>3.5[a]	4.7[b]	<1.2	0.19[c]
CAS(4/4)	4.10	6.32	2.22	0.44
CAS(6/6)	4.55	6.33	1.78	1.31
CAS(8/7)	4.50	6.26	1.76	1.89
CAS(10/8)	4.13	5.67	1.55	0.51
CAS(14/12)	4.31	5.70	1.39	1.55
MRSDCI(4/4)	4.16	5.75	1.59	0.35
MRSDCI(6/6)	4.21	5.64	1.43	0.36
MRSDCI(8/7)	4.18	5.72	1.54	0.49
MRSDCI(10/8)	4.24	5.35	1.11	0.35
EOM-CCSD	4.21	5.26	1.04	-

[a] Adiabatic excitation from ref 18. [b] Reference 16. [c] Benchmark theoretical value from ref 35.

TABLE 3: As in Table 2, but with S_0 Minimum Optimized Using CAS Instead of BLYP

	ΔE_{10}	ΔE_{20}	ΔE_{21}	S_0 barrier
CAS (4/4)	4.35	6.78	2.43	0.61
CAS (6/6)	4.64	6.89	2.25	1.49
CAS (8/7)	4.07	6.99	2.92	1.53
CAS (10/8)	4.23	6.31	2.08	0.61
CAS (14/12)	4.53	6.29	1.76	1.85

calculations will thus be that optimized with BLYP, whereas all other points are optimized at the CAS level. The validity of this procedure will be examined below.

A survey of excitation energies and barrier heights is shown in Table 2, in which the results of various CAS active spaces are compared to MRSDCI, EOM-CCSD, and experimental and theoretical benchmarks. Electrons in the five lowest energy molecular orbitals (corresponding to 1s orbitals on heavy atoms) are not correlated in MRSDCI calculations using the (10/8) active space. The experimental excitation energy for S_1 is actually the 0−0 line (adiabatic excitation) and should thus be taken as a lower bound to the vertical excitation energies to which it is compared. The S_2/S_1 energy difference given in the table then serves as an upper bound. The reference value for the S_0 proton-transfer barrier is taken from the G2 calculations[37] of Barone.[35]

The S_2/S_1 gap at the Franck−Condon point ($\Delta E_{S_2/S_1}$) systematically drops as the size of the active space is increased. Judging by the consistency of the MRSDCI values for the S_1 vertical excitation energy ($\Delta E_{S_1/S_0}$), static correlation effects at the S_1 FC point appear to be saturated even at the (4/4) level. More pronounced variation in the S_2 vertical excitation energy is observed, especially when the active space is increased to (10/8).

The trend observed for the S_0 barrier heights stands in contrast with that of the excitation energies—increasing the size of the active space substantially heightens discrepancy with the benchmark. Large active spaces result in more open minima and thus strongly destabilize the transition state. The failure of large active spaces to yield accurate barrier heights illustrates a danger of naïve active space selection based solely upon size criteria. As was the case with the excitation energies, the quality of (10/8) appears to be anomalously good and probably reflects a local minimum in the oscillatory convergence of the CAS error. Likewise, the stability of the MRCI barrier heights again points to the sufficiency of the underlying (4/4) active space for ground-state recovery of static correlation.

Table 3 shows the same results when all structures are optimized at the CAS level. CAS optimization of the ground state grossly exacerbates the balance in treatment of the excited states, as reflected in the uniformly larger values for ΔE_{21}. Aside from the anomalously bad behavior of (8/7), the trend of active space and energy gap is the same as with the previous procedure. Again with the exception of the (8/7) active space, use of a CASSCF optimized minimum results in a positive correction of 0.1−0.35 eV from the barrier height predicted using a minimum optimized at the BLYP level. We conclude from the general consistency of the trends, however, that the qualitative conclusions with respect to active space selection are unaffected by use of a BLYP starting point for dynamics.

Given the need to choose between accurate Franck−Condon gaps versus accurate barrier heights, we opted in favor of the latter. This is justified on dual grounds. The first is that such a choice increases the likelihood of accurate dynamics for the initial state, S_2. In addition, test dynamics run on the (4/4) PES encountered regions of S_2/S_1 degeneracy within a mere 10 fs of being launched from the FC region; thus the size of the initial gap reduces ultimately to a choice concerning the amount of kinetic energy to be expected following quenching to S_1. Based upon these observations, the ensuing PES characterization and dynamics will be carried out with the (4/4) active space.

As alluded to previously, inclusion of the σ^* orbital was judged an essential element in past work. The specific context was a proposed relaxation mechanism in which symmetric (C_{2v}) proton detachment lowered the energy of the $\pi\sigma^*$ state enough to intersect both $\pi\pi^*$ and ground states. This channel corresponds to motion along H_+ in Figure 1 of ref 12 (corresponding to a symmetric detachment of the hydrogen atom from the molecule) and has been referenced in experimental work on related ESIPT systems[25,26] (however, note that the findings of ref 25 do *not* support this proposal because no isotope effect was observed). Although it is obviously true that inclusion of the σ^* orbital would be essential to a proper description of hydrogen atom detachment, it simply is not relevant to S_2 photochemistry unless excitation is accompanied by a great deal of excess energy. This is actually already apparent from the results of ref 12, where it is shown that extension along the H_+ coordinate leads to an increase in the energy on S_2. By the time the energy begins to decrease again due to crossing with the $\pi\sigma^*$ state, the energy has increased by more than 0.5 eV compared to the Franck−Condon point. Access to a possible intersection is made even less likely given the presence of alternate channels presenting no energy barrier at all (as is shown to be the case below). Because the barrier to this particular channel is present with or without inclusion of the σ^* orbital, we deem its inclusion nonessential to an accurate depiction of the dynamics.

A catalog of stationary point geometries obtained with CAS-(4/4) is shown in Figure 3. The structures listed as transition states were optimized in C_{2v} (S_2) or C_2 (S_1) symmetry. As can be seen, the ground-state minimum exhibits a well-defined bond alternation pattern. The nature of $n \rightarrow \pi^*$ excitation is to transfer electron density from the oxygen lone pair (where it is favorable to hydrogen bonding) to an antibonding orbital localized along the backbone. It is not surprising then to find the S_1 minimum exhibiting substantial ring relaxation, a profoundly weakened H-bond, and decreased bond alternation. Noting also the similarity in structure of the transition states for the ground and first excited state (the S_1 structure is slightly tighter), it is to be expected that the energetic cost of moving from minimum to transition state will be much greater on S_1 than S_0. In contrast, $\pi \rightarrow \pi^*$ excitation leaves electron density along the H-bond intact, restricted instead to disruption of the bonding pattern along the backbone. Minimization of S_2 in C_{2v} symmetry yields

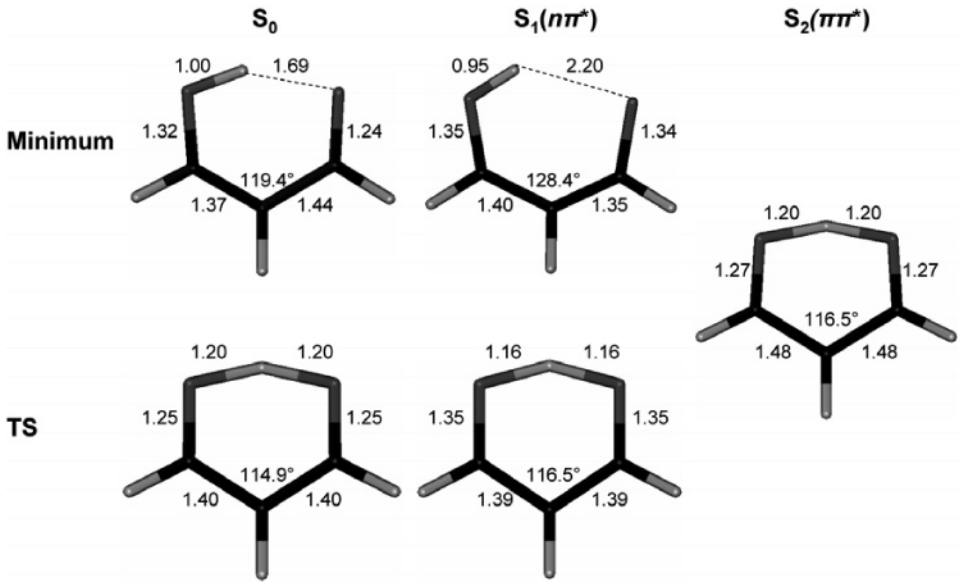

Figure 3. Geometries of minima and transition states for the ground and two lowest singlet excited states, computed with SA-3-CAS(4/4)/6-31G*. On S_1, n → π^* excitation depletes electron density along the H-bond and destroys the bond alternation pattern of the backbone, resulting in a highly relaxed minimum and thus a larger barrier to hydrogen transfer. On S_2, n → π^* excitation further weakens bond alternation of the backbone while leaving the H-bond intact, stabilizing contraction of the chelate ring and resulting in a C_{2v} planar minimum.

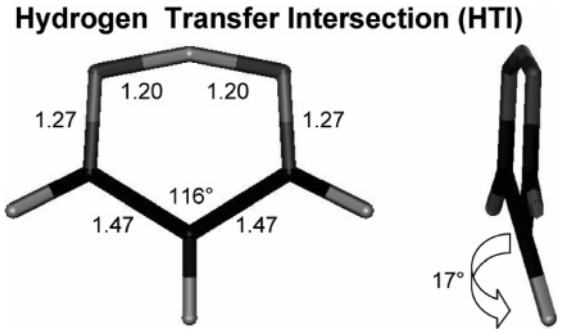

Figure 4. Hydrogen-transfer S_2/S_1 conical intersection. Bond lengths and angles for the HTI are virtually identical to those of the S_2 minimum/transition state, the only geometrical difference being slight out-of-plane distortion of one of the hydrogen atoms.

the structure shown in Figure 3, and this is unchanged by relaxation to C_2. Thus hydrogen transfer is barrierless on S_2.

Conical intersections are known to mediate nonadiabatic transitions in photochemistry, and it is thus interesting to locate the minimal energy geometries along such intersection seams. We have found three such minimal energy conical intersections (MECIs), involving S_0, S_1, and S_2. All three of these were found using SA-3-CAS(4/4) wave functions with the unconstrained algorithm of ref 38, as implemented in MolPro. These MECI geometries are shown in Figures 4 and 5. Past results[12] suggested the presence of an S_2/S_1 conical intersection near the C_{2v} configuration. We have located this MECI—a hydrogen-transfer intersection (HTI) lying energetically very close to the transition state (see also Figure 8). The only structural difference at the (4/4) level is mild out-of-plane displacement in the hydrogen bonded to the middle carbon, the C_{2v} minimal energy structure, and HTI MECI geometries being practically isoenergetic (a fact that will emerge as a key feature in the dynamics). Larger active spaces predict slight variations on this structure, although all retain the MECI's close proximity (in coordinate space) to the transition state. The key feature is the energetic relationship between the two points, as lowering the intersection relative to the transition state (for instance) may have a substantial impact on the ratio of intrastate hydrogen transfer to quenching (and interstate transfer). The energetic proximity of the S_2/S_1 HTI MECI and the putative C_{2v} transition state are retained upon addition of dynamic correlation with MRSDCI for both CAS-(4/4) and CAS(10/8) wave functions.

In addition to the HTI MECI, 90° twisting of the C═C bond leads to the global S_2 minimum, which is a simultaneous conical intersection of the three lowest singlet states (3SI). This is depicted in the left panel of Figure 5. To ensure that this somewhat remarkable occurrence was not merely an artifact of our electronic structure method, we optimized the intersection again at the SA-3-CAS(4/4)*SDCI level using a new intersection search method we recently developed.[39] This method uses numerical derivatives of the potential energy surfaces (central differences with a step size of 0.01 bohr) and does not require knowledge of the nonadiabatic coupling vector. For this optimization, the lowest seven orbitals were left doubly occupied in all configurations. The S_2/S_0 gap is 0.05 eV using the SA-3-CAS(4/4) wave function and is increased only slightly to 0.09 eV after optimization at the SA-3-CAS(4/4)*SDCI level. The final geometries are superimposed for comparison in Figure 6. Approach to the 3SI is barrierless on S_2, but the 3SI lies above the S_1 minimum by roughly 0.4 eV.

There are relatively few other reported examples of three-state conical intersections. Previous examples either were required by symmetry[40] or could be understood as arising from the triple degeneracy of the atomic p orbitals.[41−45] In the present case, neither of these considerations apply and we therefore comment on the origin of the 3SI. We have outlined in a previous publication[24] our reasons for believing that finding a 3SI may not be so surprising and provided a first glimpse of dynamics in its vicinity. For α,β-unsaturated enones such as MA and members of the salicylic acid (SA) family (cf. Figure 1), rotation about the C═C bond lowers the energy of the doubly excited $\pi^*\pi^*$ state and raises the energy of the ground state. On the other hand, the energy of the nπ^* state is expected to be significantly less affected by this torsion. When the nπ^* state lies roughly halfway between the $\pi\pi$ and $\pi^*\pi^*$ states at the Franck−Condon point, one can therefore expect that all three diabatic states will become near degenerate at the 90° twisted geometry. Small geometrical perturbations may then produce

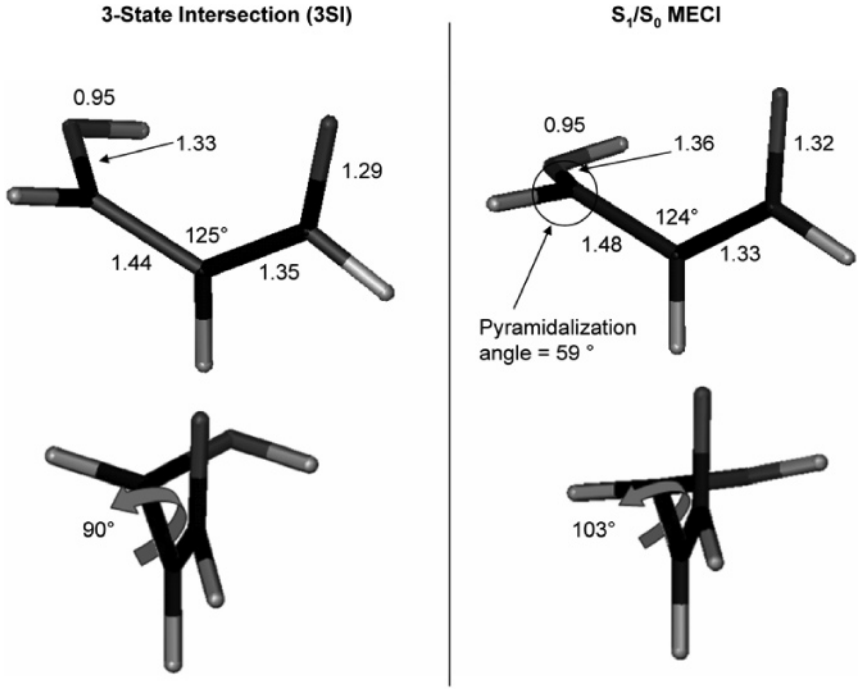

Figure 5. Twisted intersection geometries. The three-state intersection (3SI) is a simultaneous degeneracy of S_0, S_1, and S_2, characterized by 90° twisting about the C═C bond. It is the global minimum on S_2 and creates the possibility of direct relaxation from S_2 to S_0. The S_1/S_0 minimal energy intersection (MECI) is produced by additional twisting and pyramidalization of one of the carbon atoms.

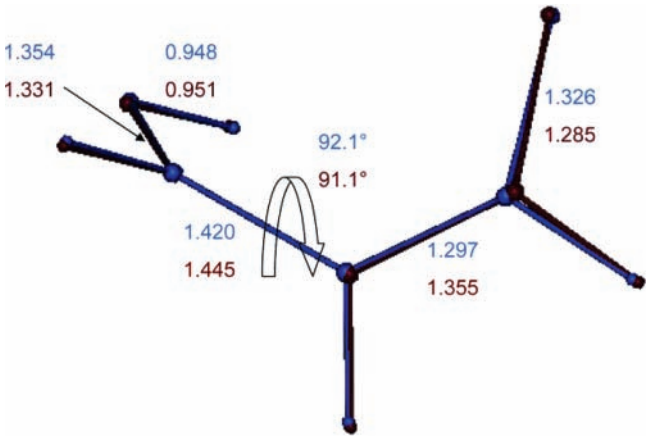

Figure 6. Comparison of SA-3-CAS(4/4) (red) and SA-3-CAS(4/4)-*SDCI (blue) 3SI geometries. Apart from minor changes in bond lengths, the structures are nearly identical.

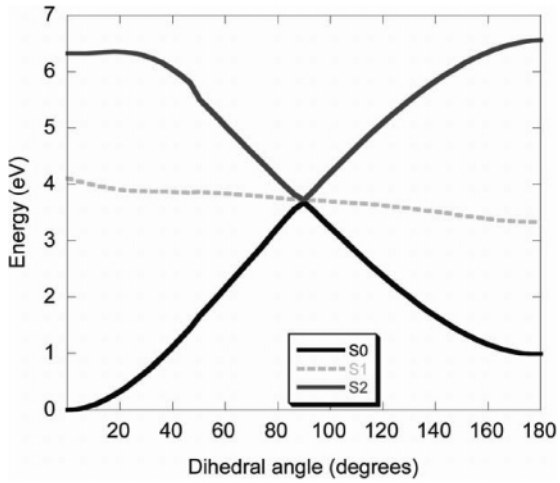

Figure 7. Behavior of potential energy surfaces expected upon torsion about the C═C bond in an α,β-unsaturated enone. Traces shown are computed for MA by rigid rotation around the C═C bond with other internal coordinates chosen to coincide with the 3SI using SA-3-CAS-(4/4) and a 6-31G* basis set. Achieving this degeneracy requires that the $n\pi^*$ state be roughly halfway between the ground and $\pi^*\pi^*$ states at the Franck−Condon point (the $\pi^*\pi^*$ at 0° twist angle correlates to the ground $\pi\pi$ state at 180° twist angle). In this case, torsion by 90° will lead to near-degeneracy of three states. Minor changes in other coordinates (such as C═O and C═C bond length) will then likely lead to a simultaneous crossing of the three diabatic states. The coupling matrix elements must also vanish; hence the existence of a three-state intersection is not guaranteed.

exact degeneracy of the three diabats. Because the conditions for a 3SI also include simultaneous vanishing of the three matrix elements that couple the diabatic states, the presence of a 3SI cannot be guaranteed even when the energetic placement of the $n\pi^*$, $\pi\pi$, and $\pi^*\pi^*$ states is favorable at the FC geometry. Figure 7 shows the result of driving the dihedral angle through the 3SI and around to the minimized 180° conformer, illustrating the basic idea of the origin of the 3SI. The impact of the 3SI upon MA photodynamics will be explored in much greater detail below.

Finally, pyramidalization of one of the carbon atoms yields the minimal energy S_1/S_0 intersection (MECI), as shown in the right panel of Figure 5. This change induces considerable separation of S_2 and S_1 but may be performed without disrupting the S_1/S_0 portion of the 3SI degeneracy (see Figure 12). Defining the pyramidalization angle τ as

$$\tau = \cos^{-1}((\vec{e}_{C_1O_4} \times \vec{e}_{C_1H_7}) \cdot \vec{e}_{C_1C_2}) \qquad (1)$$

where $\vec{e}_{xy}$ is a unit vector connecting atoms x and y, we find $\tau = 59°$ for this MECI geometry. Using a similar definition, the pyramidalization angle for an idealized sp^2 carbon atom, e.g., in ethylene, would be 0° and that for an idealized sp^3 carbon atom, e.g., in methane, would be 70.5°. This pyramidalization distortion, known as "sudden polarization" in earlier literature,[46] is the result of charge localization on the central carbon atom. It appears to be a common motif in MECI geometries for

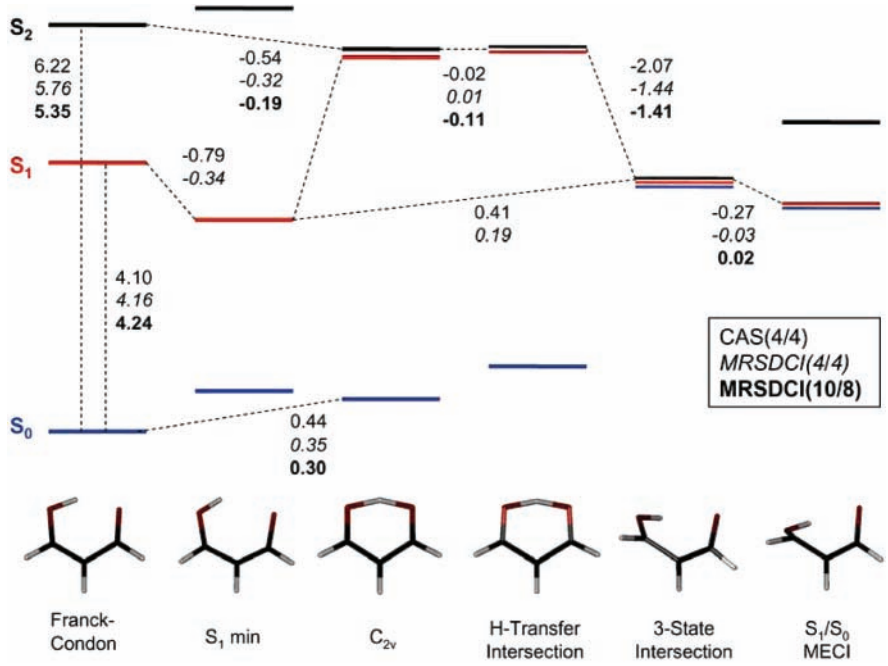

Figure 8. Energy differences (eV) between important geometries of malonaldehyde obtained using SA-3-CAS(4/4), SA-3-CAS(4/4)*SDCI (italics), and SA-3-CAS(10/8)*SDCI (bold). Geometries are determined by optimization with SA-3-CAS(4/4). S_2 excitation leads to an energetically favorable route to rotamerization that may or may not be accompanied by hydrogen transfer. The S_1-transfer barrier is quite large, and approach to the 3SI from the minimum on this state is unfavorable. Energy orderings are not significantly affected by the addition of dynamic correlation. Intersections are shown with thin lines and degenerate states slightly displaced for visual clarity.

photoisomerization processes, as reflected in high-level ab initio results for ethylene and stilbene.[47,48]

An energy level diagram in Figure 8 summarizes and relates these various points. All geometries in this figure are determined by optimization at the SA-3-CAS(4/4) level, and energies are subsequently computed with SA-3-CAS(4/4)*SDCI (italics) and SA-3-CAS(10/8)*SDCI (bold) to determine the impact of an improved treatment of electron correlation. The energetic ordering of the structures is not significantly affected by improved treatment of electron correlation or extension of the active space, verifying the SA-3-CAS(4/4) picture of the ground- and excited-state potential energy surfaces.

It is worth emphasizing that only some of the energy differences recorded in Figure 8 correspond to barrier heights. In particular, the net difference of 0.16 eV (at the SA-3-CAS-(4/4)*SDCI level) between the S_1 minimum and the S_1/S_0 MECI should not be taken as the energy required to open this relaxation channel. When ref 18 reports vibronic bands extending 5000 cm^{-1} (~0.6 eV) from the S_1 origin, it is reasonable to assume that this number represents the true barrier for which we calculate only the end points.

III. Dynamics

We carry out simulations of dynamics in MA using the full multiple spawning (FMS) method, which describes the nuclear wave function explicitly and allows for quantum mechanical nonadiabatic effects that induce population transfer between electronic states. The nuclear wave function on the *I*th electronic state, χ_I, is expanded in a series of multidimensional complex Gaussian basis functions parametrized by mean position ($\bar{R}$) and momentum ($\bar{P}$) vectors for each degree of freedom.

$$\chi_I(R;t) = \sum_{j=1}^{N_I(t)} C_j^I(t) G_j^I(R;\bar{R}_j^I(t),\bar{P}_j^I(t),\gamma_j^I(t),\alpha_j^I) \qquad (2)$$

where the upper limit N_I(t) denotes the fact that the number of basis functions associated with each electronic state changes during the dynamics. In addition to $\bar{R}$ and $\bar{P}$, the nuclear basis functions are characterized by width α (which can be different for each degree of freedom) and phase γ. The widths are held constant (the frozen Gaussian approximation[49]), and the phases evolve according to the usual semiclassical prescription, i.e., as time integrals of the Lagrangian. The coefficients C_j are propagated with the time-dependent Schrödinger equation, guaranteeing that the method becomes exact in the limit of an infinite basis. Its accuracy, then, depends on proper placement of the basis functions in phase space. Motivated by the semiclassical, short-time limit, the centroids of the nuclear basis functions follow classical trajectories. As a direct consequence, only local information (i.e., energies and gradients) is required for propagation of the basis functions and the required matrix elements of the potential energy surface can be evaluated with saddle-point approximations motivated by the localized nature of the basis functions.

At each time step, the nonadiabatic coupling between electronic states φ_J and φ_I

$$d^{JI} = \left\langle \varphi_J \left| \frac{\partial}{\partial R} \right| \varphi_I \right\rangle_r \qquad (3)$$

where the subscript *r* denotes integration over the electronic coordinates, is monitored such that values exceeding a user-defined threshold (established through preliminary testing) signal the start of a "spawning" region. The spawning procedure creates a new basis function, having the same classical energy as its "parent," on the electronic state to which the current propagation is strongly coupled. Conservation of energy is maintained through the semiclassically motivated[50] adjustment to the momentum in the direction of the nonadiabatic coupling vector. In this manner the basis set is expanded to cover regions of phase space inaccessible to conventional ab initio MD methods such as Car-Parinello,[51] and population flow is unimpaired by artificial restriction to a single electronic surface. More intimate

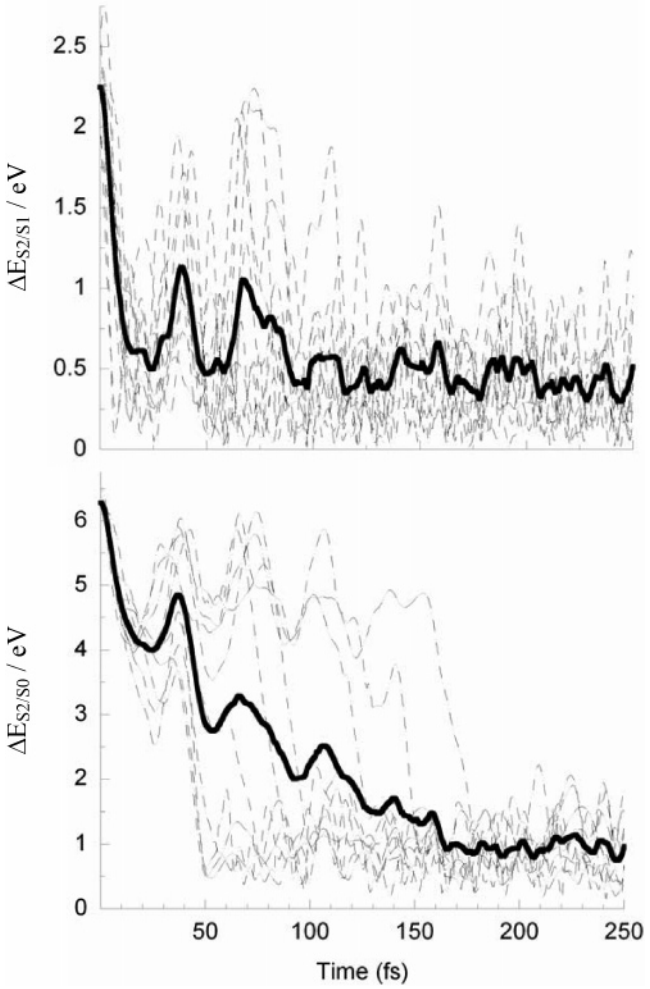

Figure 9. Evolution of S_2/S_1 (top) and S_2/S_0 (bottom) energy gaps for trajectory basis functions whose initial conditions were sampled from a Wigner distribution. Ten representative traces are shown (light gray, dotted), as well as the average over twenty trajectory basis functions (black, solid). All basis functions evolve toward S_2/S_1 near-degeneracy (nontwisted intersections) within 50 fs and reach the 3SI within 175 fs. Apart from brief intervals of twisting to 180°, trajectory basis functions entering the 3SI region on S_2 never exit.

details of the propagation, along with considerable discussion and justification of the hierarchy of approximations involved, may be found in a number of review articles.[29−31]

Dynamics results are reported for an ensemble of 20 parent trajectories (i.e., their propagation took place entirely on S_2) whose initial conditions were Monte Carlo sampled from a harmonic ground-state ($\nu = 0$) Wigner distribution.[52] In accordance with the conclusions detailed above, this distribution was centered at the BLYP S_0 minimum and the BLYP S_0 harmonic frequencies were used to generate the appropriate Wigner distribution. A velocity Verlet integrator[53] was used to perform propagation with ∼0.5 fs time steps for a total of 250 fs. The widths for the trajectory basis functions are chosen to be 6, 30, and 30 bohr^{-2} for H, C, and O atoms, respectively. The initial trajectories were not coupled to one another, but each parent trajectory was coupled to all those that it spawned. Coupling thresholds were chosen so as capture the temporally localized peaks in the nonadiabatic coupling, determined by preliminary testing. One new basis function was spawned per nonadiabatic interaction region. Basis functions with coefficients $|c_i|^2 < 0.1$ were not allowed to spawn.

We now turn to the results of the AIMS simulations. Figure 9 depicts evolution of the S_2/S_1 and S_2/S_0 energy gaps along

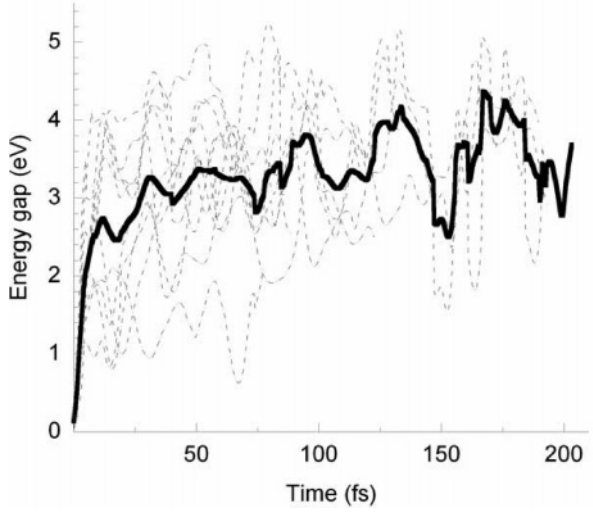

Figure 10. Evolution of S_2/S_1 energy differences for 10 representative trajectory basis functions spawned to S_1 (solid line is the average over all trajectory basis functions). The gaps rapidly become large, reflecting the redirection of S_1 population away from the 3SI. The zero of time represents the moment of basis function creation ("spawning").

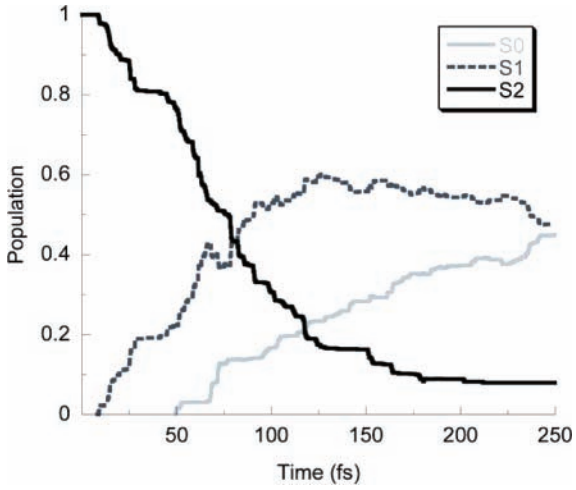

Figure 11. Population dynamics for 20 initial trajectory basis functions propagated using AIMS with SA3-CAS(4/4) electronic wave functions. Electronic relaxation from the spectroscopic bright state begins within 10 fs and is roughly complete within 200 fs. Ground-state recovery begins at 50 fs after the wave packet begins to access the 3SI.

the centroids of trajectory basis functions evolving on S_2. As noted previously, points of S_2/S_1 degeneracy are accessed within 10 fs. These roughly planar intersections are of hydrogen-transfer character, as will be reexamined below. The S_2/S_0 gap falls below 1 eV within 45−185 fs (95 fs average). We arbitrarily choose the value of 1 eV as the fiducial value signaling entrance to the 3SI region. This time range serves as a lower bound on that required to break the intramolecular H-bond and commence twisting and an upper bound on the time when hydrogen atom transfer on S_2 is possible. Once the 3SI region is entered, the average S_2/S_0 energy gaps remains near 1 eV for the remainder of the simulation. This indicates that S_2 trajectories entering the 3SI region never fully exit, as is fitting for the energetic basin surrounding the global S_2 minimum.

By way of contrast, Figure 10 illustrates S_1/S_0 gaps for a sampling of trajectories created on S_1, stemming from a mixture of spawning events originating at planar and twisted geometries. In this figure, the zero of time is defined as the first maximum in the nonadiabatic coupling between the newly spawned function and its parent. The S_2/S_1 gap becomes large within a

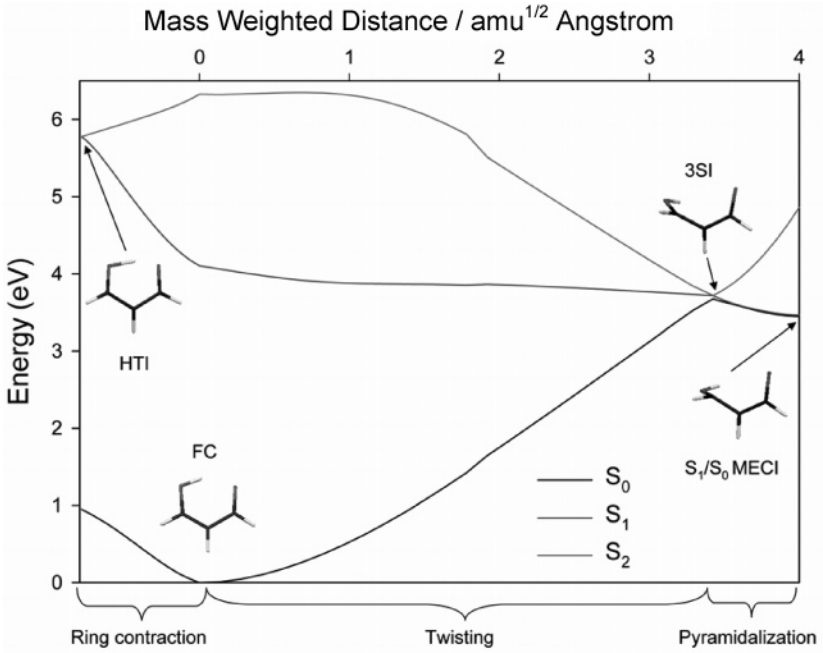

Figure 12. Ground- and excited-state potential energy surfaces along linearly interpolated (in internal coordinates) paths connecting important geometries. The *x* axis is given as mass-weighted distance and the dominant coordinate that changes along the interpolation path is indicated on the lower *x* axis. There is no barrier between the FC point on S_2 and either the HTI or the 3SI. The degeneracy of S_0 and S_1 is maintained along the interpolation path from the 3SI to the S_0/S_1 MECI. This indicates that the 3SI arises as the intersection of two seams of two-state conical intersections.

few femtoseconds of the spawning event, and this result is insensitive to the nature of the intersection (planar or twisted). This is indicative of an "inverted funnel" topography on S_1 that directs trajectory basis functions away from the intersection region, as discussed further below.

In Figure 11, we show the evolution of electronic populations predicted by the AIMS simulations. The decay of population on S_2 is almost immediate and the lifetime of S_2 can be estimated as $\approx$100 fs. Within 50 fs, significant population is accumulated on S_1 and by the end of the simulations (250 fs), the population is almost equally partitioned between S_1 and S_0. The small residual population on S_2 at the end of the simulation arises because of our imposed restriction that basis functions can only spawn when they carry sufficient population. Because the S_2 lifetime is so short and the S_1 state is spectroscopically dark, no fluorescence is expected, in accord with experiment.

Given the evident importance of the HTI, 3SI, and S_1/S_0 MECI geometries in the dynamics, we can summarize the mechanistic pathway by constructing an interpolation of the potential energy surfaces between these geometries. We use linear interpolation in internal coordinates and the resulting curves are depicted in Figure 12. Starting at the FC geometry, the molecule can proceed to either of the HTI or 3SI geometries. As the slopes of the curves in Figure 12 suggest, it is more likely that the molecule proceeds toward the HTI, at least initially. This is also indicated by the evolution of the S_2/S_1 and S_2/S_0 gaps presented in Figure 9. In fact, it is possible to proceed from the HTI to the 3SI, and this is what we generally observe. Once the 3SI is encountered, passage to the S_1/S_0 MECI is barrierless and the degeneracy between S_1 and S_0 is not lifted along the linear interpolation path. This highlights the (N-5)-dimensional 3SI as the confluence of two $(N-2)$-dimensional seams, one of which includes the S_1/S_0 MECI. It is likely that the other seam includes the S_2/S_1 HTI geometry. The 3SI is then likely a minimum on the S_2/S_1 seam and a maximum on the S_1/S_0 seam.

Schematically, then, the dynamics consists of ring contraction (FC to HTI) followed by torsion (HTI to 3SI) and pyramidalization of a carbon atom (3SI to S_1/S_0 MECI). Hydrogen atom transfer can and does occur, but we first focus on the novel feature of dynamics around a 3SI. Given the presence of a 3SI, one might expect to observe significant quenching directly from S_2 to the ground state. However, only 4 out of 256 total spawns take place directly from S_2 to S_0 in the 250 fs examined. Of these, only one takes any population, and in that case only 1%. This suggests that population decays sequentially from S_2 to S_1 and then from S_1 to S_0 despite the proximity to the 3SI. Although initially surprising, perhaps this result is to be expected. Absence of significant relaxation directly from S_2 to S_0 is best understood in terms of the dimensionality difference between the 3SI branching space and that of a conventional two-state conical intersection.[24] The degeneracy of two states is broken in two dimensions, but that of three is broken in five. As the wave packet approaches the 3SI, it is continually coming in contact with two-state intersections. Rather than a large degree of direct quenching, then, one would expect spawning events to be located all along the approach to the 3SI itself.

The histogram shown in Figure 13 confirms this suspicion. Here we show the distribution of energy gaps for both twisted ($\angle O_4C_1C_2H_8 \geq 60°$, designated as 3SI in the figure) and nontwisted (designated as HTI in the figure) spawning geometries. "Spawning geometries" are defined as the geometries where the nonadiabatic coupling increased above the spawning threshold and a new basis function was created. These are a useful device for analysis of the dynamics, but we remind the reader that population transfer occurs over a finite time duration and that the amount of population transfer is determined by the integration of the nuclear Schrödinger equation. The use of "spawning geometries" in the analysis should not be taken to imply that population transfer only occurs at these specific geometries. The distribution of S_2/S_0 gaps (which, unlike the S_2/S_1 gaps, continue on to higher energies) is much wider than those for S_2/S_1 around either the 3SI (twisted geometries) or the HTI (near-planar geometries), indicating nonadiabatic S_2/S_1 interaction all along the path of approach to the 3SI. The black bars are for spawning events where the geometry is nearly

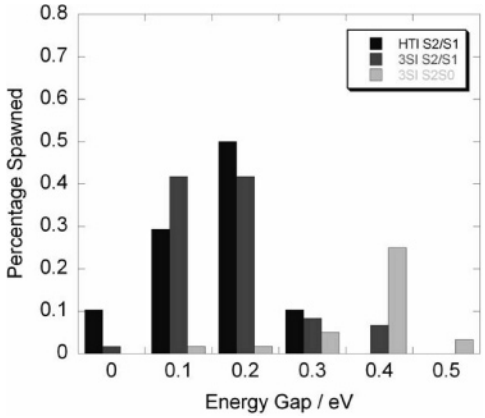

Figure 13. Histogram of S_2/S_0 (light gray) and S_2/S_1 (dark gray and black) energy gaps for spawning events from trajectory basis functions on S_2. The black bars correspond to spawning events in which the geometry is nearly planar; i.e., those occurring near the HTI MECI. S_2/S_0 gaps for these geometries always exceed 3 eV and are not depicted. The dark and light gray bars represent energy gaps for spawning events in which the geometry is strongly twisted about the C═C bond, i.e., near the 3SI. Notice that the distribution of S_2/S_0 gaps is broad compared to either of the S_2/S_1 energy gap distributions, in addition to being peaked further from 0 eV. This indicates that even in the vicinity of the 3SI, population transfer is generally mediated by two-state conical intersections.

planar, i.e., near the HTI MECI. S_2/S_0 gaps for these geometries always exceed 3 eV, as one would expect from Figure 12. The dark and light gray bars represent energy gaps for spawning events where the geometry is strongly twisted about the C═C bond, i.e., near the 3SI. Notice that the distribution of S_2/S_0 gaps is broad compared to either of the S_2/S_1 energy gap distributions and is furthermore centered at higher energy. Therefore, quenching in the vicinity of the 3SI actually occurs before the simultaneous triple degeneracy is reached, and the quenching behavior is similar to that expected if there were two closely spaced S_2/S_1 and S_1/S_0 conical intersection seams.

As was already seen in Figure 10, quenching to S_1 diverts population away from the 3SI. Figure 14 shows the potential energy surface topography in the neighborhood of the 3SI. Although the actual 3SI branching space is 5-dimensional, we have chosen a 2-dimensional cut composed of bond alternation and twisting about the C═C bond. The intersection has a strong funnel character on S_2, and the S_1/S_0 degeneracy is not completely lifted for the portion of the branching space shown. The arrows drawn on the surface indicate schematically the observed behavior—population which quenches to S_1 or S_0 near the 3SI rapidly leaves the region of simultaneous triple degeneracy.

To better characterize dynamics on each of the potential energy surfaces, we computed one-dimensional reduced densities along an internal coordinate corresponding to hydrogen transfer. The oxygen atom to which the labile hydrogen atom is initially bonded is denoted as O_d (donor), and the other oxygen atom is labeled as the acceptor (O_a). The difference of the O_a-H and O_d-H distances (labeled AH−DH in Figure 15) is then a measure of hydrogen transfer. Large values (greater than 1 Å) signal twisting about the C−C bond and opening of the chelate ring. The remaining degrees of freedom were integrated out using an importance-sampled Monte Carlo procedure. The integrals were performed with 100 000 sampling points, and the results are shown in Figure 15.

Population on S_2 is significantly depleted prior to wave packet bifurcation as a result of twisting (bottom), and segregation into reactant and product wells is visible on all states within the first 100 fs. Quenching to S_1 proceeds with significant momentum along the rotamerization coordinate, and the AH−DH distance reaches a mean absolute value of ∼4 Å within 150 fs. Progression along this mode is likewise reflected in the faint traces of residual population on S_2. The opening of the chelate ring prevents any subsequent hydrogen transfer on S_1 and S_0. Concentration of density in the reactant region shows that ESIPT is not strongly favored, and all of the population has undergone twisting by 200 fs.

To further clarify ESIPT at early times and quantify the extent of reaction, we also partially integrated the above densities over the hydrogen-transfer coordinate. We define the extent of hydrogen transfer by introducing a dividing surface separating reactants and products at

$$R = R_{AH} - R_{DH} = 0 \tag{4}$$

in which R_{DH} and R_{AH} denote hydrogen-donor and hydrogen-acceptor distances, respectively. The extent of reaction (transferred hydrogen, H_T) is then defined as the expectation value of a projection operator

$$H_T = \langle \psi | \hat{P}^2 | \psi \rangle \tag{5}$$

in which the projection operator is the Heaviside step function, $\hat{P} = \theta(R)$. This integral is then evaluated in the manner described above and untransferred hydrogen is defined simply as $H_U = 1 - H_T$.

Figure 16 shows (on each electronic state) the time evolution of the fraction of the wave packet for which the hydrogen atom remains bound to O_d, i.e., untransferred hydrogen H_U. Hydrogen atom transfer begins almost instantaneously after photoexcitation, as does population transfer from S_2 to S_1 (see Figure 11). This coincidence of electronic quenching and hydrogen atom transfer is expected due to the close proximity of the HTI MECI and the C_{2v} geometry that defines the dividing surface. This feature should be expected in any ESIPT molecule where an $n\pi^*$ state lies below a bright $\pi\pi^*$ state, because the energetically favorable path to hydrogen atom transfer will also lead to a diminished S_2/S_1 gap. ESIPT on S_2 is complete within ∼75 fs, and variations in H_U on S_1 are due solely to population transfer from S_2. As shown in Figure 15, roughly 70% of the final product on S_0 appears with the hydrogen bonded to the donor oxygen, i.e., with no net hydrogen atom transfer.

The interplay of electronic and nuclear dynamics is more fully illustrated in Figure 17. Here we display evolution of the electronic wave function and hydrogen transfer for a representative trajectory basis function. The HOMO and LUMO in the S_2-state-specific (*not* state-averaged) natural orbital representation are shown to the left of the plot. These do not change character significantly during the course of the dynamics, and hence only the orbitals at time $t = 0$ are shown. The natural orbitals are quite localized and correspond to opposing bond alternation patterns. The CI expansion that results is dominated by two configurations corresponding to double occupation of one or the other of the depicted orbitals. The weights for these two dominant configurations are plotted along with the hydrogen atom position (using the convention established in Figure 16). The configuration with the largest weight is always the one whose bond alternation character opposes the current position of the hydrogen atom. This is seen clearly around 40 fs, when the hydrogen atom is transferred and the weights of the two configurations are reversed. This is consistent with the fact that the minimum energy planar geometry on S_2 has the hydrogen atom equispaced between the two O atoms. As expected from

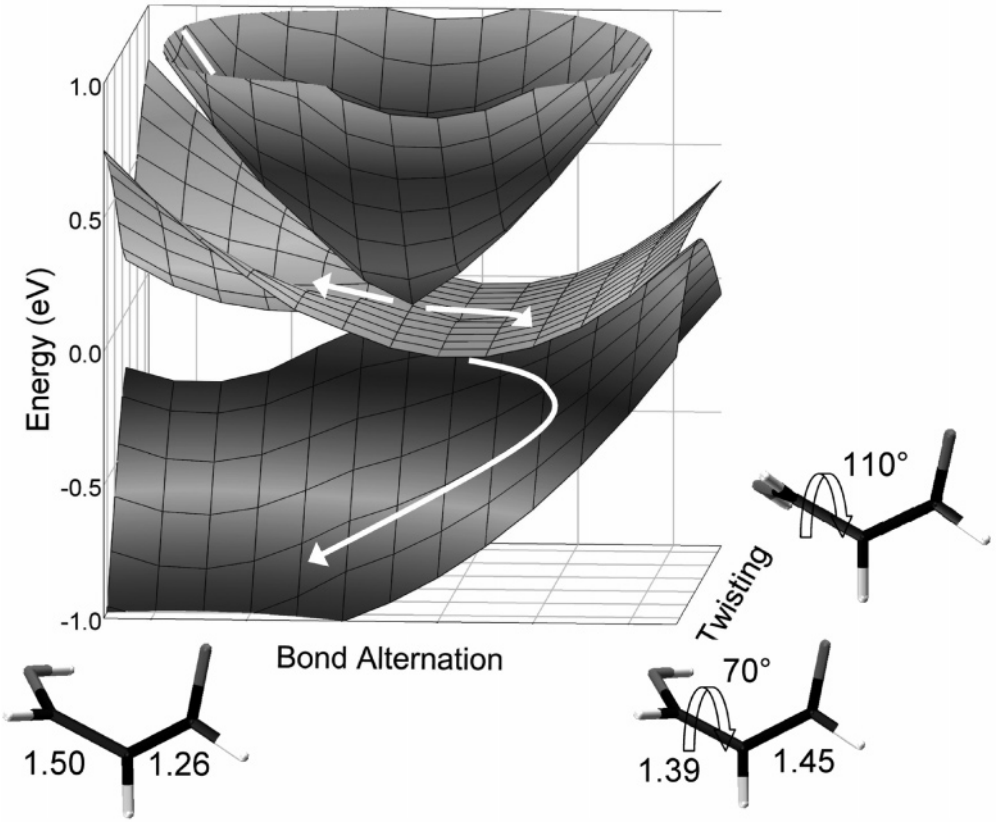

Figure 14. Potential energy surface topography in the neighborhood of the three-state conical intersection, calculated using an SA-3-CAS(4/4) wave function. The branching plane displacements correspond to bond alternation along the backbone and twisting about the C═C bond. Note that the full branching plane is five-dimensional; i.e., there are three other independent displacement directions which lift the triple degeneracy. Furthermore, there are directions that only partially lift the triple degeneracy, leaving a double degeneracy, as shown in Figure 12. The arrows indicate schematically the observed dynamics, stressing that population that decays from S_2 at the 3SI is diverted away from the simultaneous triple degeneracy.

this analysis, twisting always occurs around the C−C bond, which would be a formal double bond on S_0 given the particular position of the hydrogen atom.

IV. Concluding Remarks

We have reported ab initio molecular dynamics simulation of excited-state hydrogen transfer and three-state intersection dynamics in MA. Quantum chemistry and ab initio dynamics have been applied together to locate and refine regions of the potential energy surfaces central to excited-state evolution. These two approaches work together to produce an accurate mechanistic picture of malonaldehyde photochemistry. There are two primary decay channels after photoexcitation to the bright $\pi\pi^*$ S_2 state: (1) in-plane evolution, leading to reversible hydrogen exchange accompanied by quenching to the S_1 $n\pi^*$ state through a nearby S_2/S_1 conical intersection, and (2) torsion about the C═C bond, leading to opening of the chelate ring, which shuts off hydrogen atom transfer and leads to efficient quenching to both S_1 and S_0 through a three-state $S_2/S_1/S_0$ conical intersection. It is expected that the balance between these channels can be altered by increasing the energy in out-of-plane modes, for example, by ground-state pumping or simply raising the temperature. Alternatively, the hydrogen-atom-transfer channel could be favored by slowing down C═C torsion in a viscous solvent environment.

Because salicylic acid (SA) and its derivatives (see Figure 1) all contain the chelate ring as a major structural component, it is expected that some features of MA structure and dynamics will be paradigmatic for this family of molecules. Two key differences in these related ESIPT molecules can be noted. First, the ordering of the nπ^* and $\pi\pi^*$ states will be significantly affected by the presence of electron-withdrawing or electron-donating substituents. When the $n\pi^*$ state lies above the $\pi\pi^*$ state in the Franck−Condon region, as is the case in methyl salicylate (MS), the three-state intersection will no longer be energetically accessible after $\pi \rightarrow \pi^*$ excitation (and may not even exist). However, even when the $n\pi^*$ state lies above the $\pi\pi^*$ state there will be a *two-state* conical intersection again resulting from C═C torsion, analogous to the 3SI described here.

Second, the mass of substituents in larger molecules may tip the kinetics to favor a greater percentage of ESIPT prior to twisting (if such motion is available at all). When there is a barrier to C═C torsion, this would lead to a threshold behavior for fluorescence based on excess energy. Indeed, this was observed for MS[27] and the dynamics results presented here suggest that rotamerization is responsible for the loss of fluorescence at higher excess energies in MS. It would be interesting to determine whether 7HIN exhibits similar decay behavior, for in this case the analogous twisting mode should be largely suppressed as a result of the molecular topology (see Figure 1).

There are a number of avenues along which the current work may be expanded. Our AIMS simulations show that the ring bending and bond alternation modes (*not* the O−H stretch, in keeping with previous experimental results on OHPP[54]) are strongly coupled to $\pi\pi^*$ excitation, but it would be useful to further quantify this by simulating resonance Raman spectra. Large breakdowns in the harmonic approximation are expected for vibrations active in what is essentially a chemical reaction, so falling frequency differences between consecutive overtones

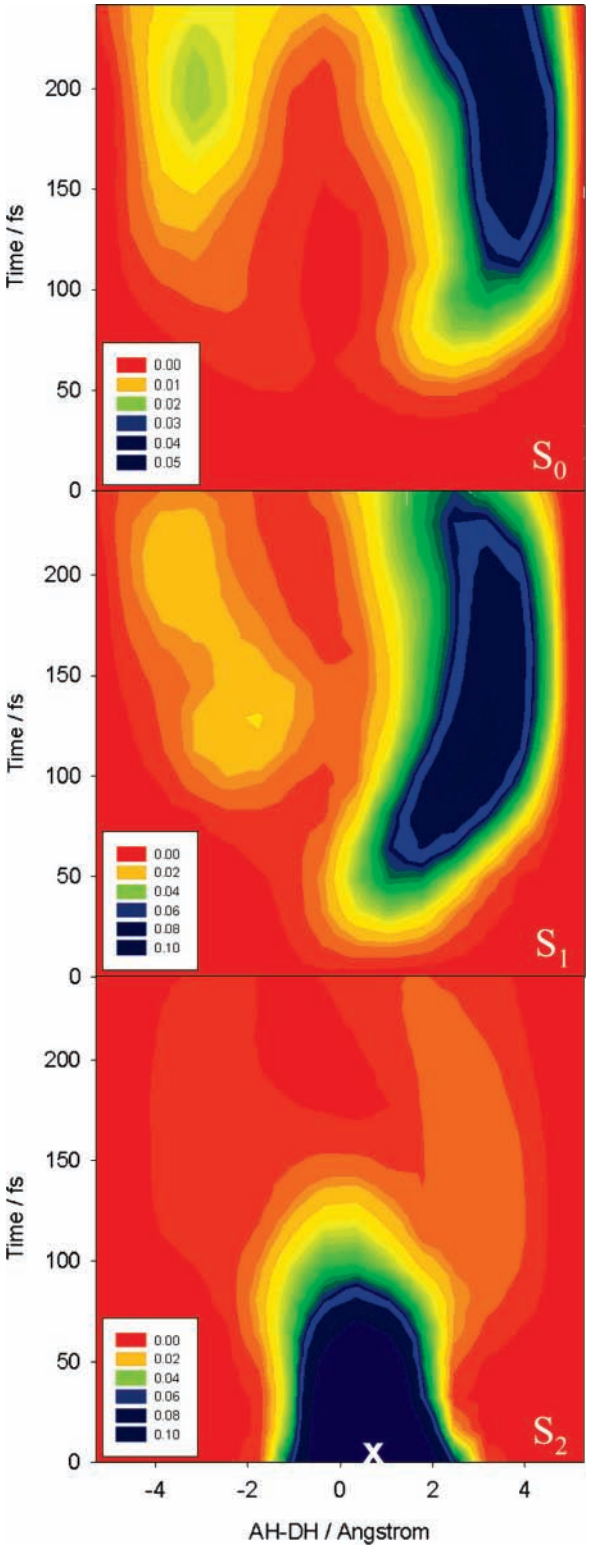

Figure 15. Reduced nuclear wave function densities along the coordinate corresponding to hydrogen transfer (the difference between acceptor-hydrogen, AH, and donor-hydrogen, DH, bond lengths). Twisting induces wave packet bifurcation on S_2 (bottom panel), although the extent of reaction is strongly limited by population quenching to S_1 (middle panel). Here rotamerization continues, preventing any further hydrogen atom transfer. The Franck−Condon point is indicated by a white "x". The calculations are all carried out in the full dimensionality of the molecule and the reduction to a single dimension is done here by Monte Carlo integration of the FMS wave function.

and enhanced intensities in combination bands would signal modes central to the exchange process.[55−57] We hope to present

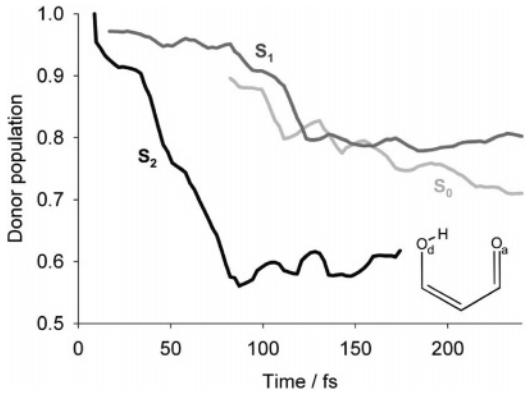

Figure 16. Hydrogen-transfer dynamics for each electronic state, showing state normalized probability of having the hydrogen atom bonded to the donor oxygen (labeled O_d in the inset). Data are shown only when there is significant (>0.1) population on the indicated electronic state. Competition with twisting strongly inhibits both forward and reverse reactions on S_2 (black). The resultant inhibition of hydrogen exchange results in most population transferred to S_1 (dark gray) having the hydrogen atom trapped on the donor side. Although the majority of population relaxes from S_1 on the donor side, the possibility of transfer reemerges on S_0 (light gray) due to the large amount of kinetic energy available.

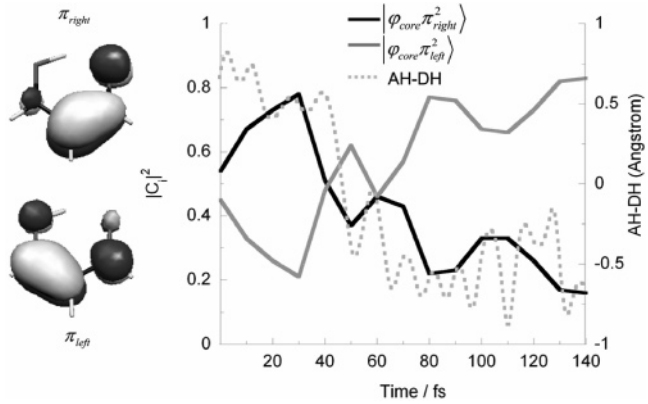

Figure 17. Interplay of electronic and nuclear dynamics for a representative trajectory. The plot shows both the time evolution of the weights (left axis) of the two dominant electronic configurations $-\pi_{right}^2$ (black) and π_{left}^2 (dark gray) and also the difference in O_a-H and O_d-H distances (right axis, light gray, dotted). The bond alternation pattern of the dominant electronic configuration always opposes the current hydrogen position. Thus the electrons are always pushing the hydrogen atom back to the symmetric position.

such an analysis for this and certain members of the SA family in a later publication.

Our discussion in this paper has so far made no reference to the conventional theory of nonradiative transitions rooted in Fermi's Golden Rule (FGR).[58,59] Though we do not wish to elaborate at length on the relationship of such theories to the current picture, which emphasizes conical intersections, a few general comments are nevertheless in order. The FGR approach is most well-suited to describing the rate of decay of the initially excited electronic state. As usually applied, it does *not* provide information about photochemical mechanisms and/or competing pathways. In contrast, the AIMS approach predicts excited-state lifetimes, photochemical mechanisms, and branching ratios for different products.

It is interesting to note the connectivity of the 3SI with the S_1/S_0 MECI, especially in light of recent work on ethylene indicating that *all* of the intersection types characterized in that system thus far actually lie on one seam.[60] This state of affairs was recently postulated more generally,[61] and there are intriguing

indicators that MA may support this conjecture. The HTI would in this event be a saddle point in an $(N-2)$-dimensional seam whose minimum is the $(N-5)$-dimensional 3SI. This point, in turn, would be a saddle point for another $(N-2)$-dimensional seam whose minimum is the S_1/S_0 MECI. The chemically relevant coordinates for moving along these seams are bond alternation, twisting, and pyramidalization. Various approaches are currently being taken to test these conjectures.

Both of the relaxation pathways examined here lead to complex S_1 dynamics that does not include additional hydrogen transfer or recrossing to S_2. The role of tunneling in S_1 dynamics is at this stage unclear, although split lines are clearly evident in direct S_1 excitation.[18,20] The multiple spawning method as used in this paper does not make any provision for adaptive increase of the basis set to describe tunneling effects. We have formulated an extended version of the method that does capture tunneling effects,[62] but it remains to be implemented in the context of ab initio multiple spawning. More detailed investigation of the S_1 dynamics in MA will be carried out when this implementation is complete.

Acknowledgment. This work was supported by the National Science Foundation (CHE-02-311876 and DMR-03-25939) with additional support through the Frederick Seitz Materials Research Laboratory (DOE DEFG02-91ER45439) at the University of Illinois Urbana-Champaign. T.J.M. is a MacArthur Fellow, Packard Fellow, and a Dreyfus Teacher-Scholar.

Supporting Information Available: Figure comparing CASSCF and MRSDCI potential energy (S_2) traces along CASSCF dynamical path and Cartesian coordinates for geometries discussed in the text, six pages. This material is available free of charge via the Internet at http://pubs.acs.org.

References and Notes

(1) Douhal, A.; Lahmani, F.; Zewail, A. H. *Chem. Phys. Lett.* **1996**, *207*, 477.
(2) Formosinho, S. J.; Arnaut, L. G. *J. Photochem. Photobiol. A: Chem.* **1993**, *75*, 21.
(3) Chou, P.; McMorrow, D.; Aartsma, T. J.; Kasha, M. *J. Phys. Chem.* **1984**, *88*, 4596.
(4) Ferrer, M. L.; Acuna, A. U.; Amat-Guerri, F.; Costela, A.; Figuera, J. M.; Florido, F.; Sastre, R. *Appl. Opt.* **1994**, *33*, 2266.
(5) Khan, A. U.; Kasha, M. *Proc. Natl. Acad. Sci.* **1983**, *80*, 1767.
(6) Werner, T. *J. Phys. Chem.* **1979**, *83*, 320.
(7) Williams, D. L.; Heller, A. *J. Phys. Chem.* **1970**, *74*, 4473.
(8) Heller, H. J.; Blattmann, H. R. *Pure Appl. Chem.* **1973**, *36*, 141.
(9) Smith, T. P.; Zaklika, K. A.; Thakur, K.; Walker, G. C.; Tominaga, K.; Barbara, P. F. *J. Photochem. Photobiol. A: Chem.* **1992**, *65*, 165.
(10) Chattoraj, M.; King, B. A.; Bublitz, G. U.; Boxer, S. G. *Proc. Natl. Acad. Sci.* **1996**, *93*, 8362.
(11) Weller, A. *Elektrochemie* **1952**, *56*, 662.
(12) Sobolewski, A. L.; Domcke, W. *J. Phys. Chem.* **1999**, *103A*, 4494.
(13) Barbara, P. F.; Walsh, P. K.; Brus, L. E. *J. Phys. Chem.* **1989**, *93*, 29.
(14) Baughcum, S. L.; Duerst, R. W.; Rowe, W. F.; Smith, Z.; Wilson, E. B. *J. Am. Chem. Soc.* **1981**, *103*, 6296.
(15) Firth, D. W.; Beyer, K.; Dvorak, M. A.; Reeve, S. W.; Grushow, A.; Leopold, K. R. *J. Chem. Phys.* **1991**, *94*, 1812.
(16) Seliskar, C. J.; Hoffmann, R. E. *Chem. Phys. Lett.* **1976**, *43*, 481.
(17) Seliskar, C. J.; Hoffmann, R. E. *J. Am. Chem. Soc.* **1977**, *99*, 7072.
(18) Seliskar, C. J.; Hoffmann, R. E. *J. Mol. Spectrosc.* **1981**, *88*, 30.
(19) Luth, K.; Scheiner, S. *J. Phys. Chem.* **1994**, *98*, 3582.
(20) Arias, A. A.; Wasserman, T. A. W.; Vaccaro, P. H. *J. Chem. Phys.* **1997**, *107*, 5617.
(21) Stanton, J. F.; Gauss, J.; Ishikawa, N.; Head-Gordon, M. *J. Chem. Phys.* **1995**, *103*, 4160.
(22) Sobolewski, A. L.; Domcke, W. *Chem. Phys. Lett.* **1993**, *211*, 82.
(23) Sobolewski, A. L.; Domcke, W. *Chem. Phys.* **2000**, *259*, 181.
(24) Coe, J.; Martinez, T. J. *J. Am. Chem. Soc.* **2005**, *127*, 4560.
(25) Lochbrunner, S.; Schultz, T.; Schmitt, M.; Shaffer, J. P.; Zgierski, M. Z.; Stolow, A. *J. Chem. Phys.* **2001**, *114*, 2519.
(26) Stock, K.; Bizjak, T.; Lochbrunner, S. *Chem. Phys. Lett.* **2002**, *354*, 409.
(27) Herek, J. L.; Pedersen, S.; Banares, L.; Zewail, A. H. *J. Chem. Phys.* **1992**, *97*, 9046.
(28) Lochbrunner, S.; Wurzer, A. J.; Riedle, E. *J. Chem. Phys.* **2000**, *112*, 10699.
(29) Ben-Nun, M.; Martínez, T. J. *J. Chem. Phys.* **1998**, *108*, 7244.
(30) Ben-Nun, M.; Quenneville, J.; Martínez, T. J. *J. Phys. Chem.* **2000**, *104A*, 5161.
(31) Ben-Nun, M.; Martinez, T. J. *Adv. Chem. Phys.* **2002**, *121*, 439.
(32) Roos, B. O. The Complete Active Space Self-Consistent Field Method and its Applications in Electronic Structure Calculations. In *Advances in Chemical Physics: Ab Initio Methods in Quantum Chemistry II*; Lawley, K. P., Ed.; John Wiley and Sons Ltd.: New York, 1987; p 399.
(33) Docken, K. K.; Hinze, J. *J. Chem. Phys.* **1972**, *57*, 4928.
(34) Werner, H.-J.; Meyer, W. *J. Chem. Phys.* **1981**, *74*, 5794.
(35) Barone, V.; Adamo, C. *J. Chem. Phys.* **1996**, *105*, 11007.
(36) Frisch, M. J.; Scheiner, A. C.; Shaefer, H. F., III; Binkley, J. S. *J. Chem. Phys.* **1985**, *82*, 4194.
(37) Curtiss, L. A.; Raghavachari, K.; Trucks, G. W.; Pople, J. A. *J. Chem. Phys.* **1991**, *94*, 7221.
(38) Bearpark, M. J.; Robb, M. A.; Schlegel, H. B. *Chem. Phys. Lett.* **1994**, *223*, 269.
(39) Levine, B. G.; Ko, C.; Quenneville, J.; Martinez, T. J. *Mol. Phys.*, in press.
(40) Katriel, J.; Davidson, E. R. *Chem. Phys. Lett.* **1980**, *76*, 259.
(41) Matsika, S.; Yarkony, D. R. *J. Chem. Phys.* **2002**, *117*, 6907.
(42) Matsika, S.; Yarkony, D. R. *J. Am. Chem. Soc.* **2003**, *125*, 10672.
(43) Matsika, S.; Yarkony, D. R. *J. Am. Chem. Soc.* **2003**, *125*, 12428.
(44) Han, S.; Yarkony, D. R. *J. Chem. Phys.* **2003**, *119*, 11561.
(45) Han, S.; Yarkony, D. R. *J. Chem. Phys.* **2003**, *119*, 5058.
(46) Salem, L. *Acc. Chem. Res.* **1979**, *12*, 87.
(47) Ben-Nun, M.; Martínez, T. J. *Chem. Phys.* **2000**, *259*, 237.
(48) Quenneville, J.; Martínez, T. J. *J. Phys. Chem.* **2003**, *107A*, 829.
(49) Heller, E. J. *J. Chem. Phys.* **1981**, *75*, 2923.
(50) Herman, M. F. *J. Chem. Phys.* **1984**, *81*, 754.
(51) Car, R.; Parrinello, M. *Phys. Rev. Lett.* **1985**, *55*, 2471.
(52) Hillery, M.; O'Connell, R. F.; Scully, M. O.; Wigner, E. P. *Phys. Rep.* **1984**, *106*, 121.
(53) Swope, W. C.; Andersen, H. C.; Berens, P. H.; Wilson, K. R. *J. Chem. Phys.* **1982**, *76*, 637.
(54) Peteanu, L. A.; Mathies, R. A. *J. Phys. Chem.* **1992**, *96*, 6910.
(55) Pfeiffer, M.; Lau, A.; Lenz, K.; Elsaesser, T. *Chem. Phys. Lett.* **1997**, *268*, 258.
(56) Pfeiffer, M.; Lenz, K.; Lau, A.; Elsaesser, T. *J. Raman. Spectrosc.* **1995**, *26*, 607.
(57) Pfeiffer, M.; Lenz, K.; Lau, A.; Elsaesser, T.; Steinke, T. *J. Raman Spectrosc.* **1997**, *28*, 61.
(58) Jortner, J.; Englman, R. *Mol. Phys.* **1970**, *18*, 145.
(59) Freed, K. F. *Acc. Chem. Res.* **1978**, *11*, 74.
(60) Barbatti, M.; Paier, J.; Lischka, H. *J. Chem. Phys.* **2004**, *121*, 11614.
(61) Martinez, T. J. *Faraday Discuss.* **2004**, *127*, 227.
(62) Ben-Nun, M.; Martínez, T. J. *J. Chem. Phys.* **2000**, *112*, 6113.